# Fluid and gyrokinetic simulations of impurity transport at JET

H. Nordman[1], A. Skyman[1], P. Strand[1], C. Giroud[2], F. Jenko[3], F. Merz[3], V. Naulin[4], T. Tala[5] and the JET-EFDA Contributors.*

JET-EFDA, Culham Science Centre, OX14 3DB, Abingdon, UK.

[1] Department of Earth and Space Sciences, Chalmers University of Technology, Euratom-VR Association, SE-412 96 Göteborg, Sweden.
[2] EURATOM/CCFE Association, Culham Science Centre, Abingdon, OX14 3DB UK.
[3] Max-Planck-Institut für Plasmaphysik EURATOM-IPP, D-85748 Garching Germany.
[4] Association EURATOM/RISO-Technical University of Denmark, Roskilde, Denmark.
[5] Association EURATOM/Tekes, VTT, P.O. Box 1000, FIN-02044 VTT, Finland.

[*] See annex of F. Romanelli et al., "Overview of JET Results", (Proc. 23rd IAEA Fusion Energy Conference, Daejeon, Korea (2010)).

## Abstract

Impurity transport coefficients due to Ion-Temperature-Gradient (ITG) mode and Trapped-Electron (TE) mode turbulence are calculated using profile data from dedicated impurity injection experiments at JET. Results obtained with a multi-fluid model are compared with quasi-linear and nonlinear gyrokinetic simulation results obtained with the code GENE. The sign of the impurity convective velocity (pinch) and its various contributions are discussed. The dependence of the impurity transport coefficients and impurity peaking factor $-\nabla n_Z/n_Z$ on plasma parameters like impurity charge number Z, ion logarithmic temperature gradient, collisionality, ExB shearing, and charge fraction are investigated. It is found that for the studied ITG dominated JET discharges, both the fluid and gyrokinetic results show an increase of the impurity peaking factor for low Z-values followed by a saturation at moderate values of impurity peaking, much below the neoclassical predictions, for large values of Z. The results are in qualitative agreement with the experimental trends observed for the injected impurities (Ne, Ar, Ni) whereas for the background carbon species the observed flat or weakly hollow C profiles are not well reproduced by the simulations.

# I. INTRODUCTION

It is well known that the presence of impurities in tokamak fusion plasmas may have a limiting effect on the performance by their contribution to radiation losses and plasma dilution resulting in lower fusion power. Impurities arise in the fusion plasma from the sputtering of the wall and divertor materials (e.g. Be, C and W), from impurity seeding in in the edge in order to reduce power loads (Ne, Ar), and from the D-T reaction in the form of He-ash. In ITER, the material configuration for the main chamber/divertor is beryllium/tungsten which will also be tested in JET as part of the ITER like wall project [1]. Accordingly, the scaling of impurity transport with impurity charge Z, from He to high Z impurities like W, is crucial for the performance and optimisation of a fusion reactor.

Impurity transport, both neoclassical and anomalous caused by turbulence, has been investigated in a number of theoretical [2-26] and experimental [27-34] studies. Theoretically, detrimental high-Z impurity accumulation is predicted in the core region by collisional transport theory [2-4]. This is usually not seen in experiments where neoclassical impurity transport coefficients are typically one or two orders of magnitude too small to explain the experimental results in the confinement zone. In this region, anomalous transport due to ITG/TE mode turbulence is expected to dominate for all channels of transport. Early studies of ITG mode driven impurity transport [12] reported an outward impurity flux for sufficiently peaked impurity density profiles, thereby avoiding severe impurity peaking in the core. In experiments it has also been observed that with the addition of ion cyclotron resonance heating to neutral beam heated discharges, accumulation of high-Z impurities can be avoided if most of the heating power is deposited on the electrons, while if the heating is deposited on the ions, the impurities accumulate in the core [31-33].

To study the Z-dependency of impurity transport in more detail, a set of dedicated impurity injection experiments has been performed at JET [33]. Extrinsic impurities were injected by laser ablation (Ni) and gas injection (Ne, Ar) and the diffusivity $D_Z$ and convective velocity $V_Z$ were determined by matching spectroscopic data with predictive results obtained with the transport code UTC-SANCO [34]. In addition, the Carbon peaking factor was determined from the background C profile.

In the present paper, background data taken from the impurity injection experiments in JET are used in interpretative transport calculations based on anomalous transport due ITG/TE mode mode turbulence. The transport coefficients are calculated using the Weiland multi-fluid model [35] which is compared and contrasted with results from quasi-linear (QL) and nonlinear (NL) gyrokinetic simulations using the code GENE [36]. In particular, the dependence of the impurity transport coefficients and impurity density peaking factor $-\nabla n_z/n_z$ on plasma parameters, in particular the impurity charge number which is varied from Z=2 to Z=74, is discussed and compared with experimental trends. The main purpose of the work is to obtain an increased understanding of impurity transport in the confinement zone of tokamaks and to quantify to what extent a computationally fast and efficient fluid model can reproduce the gyro-kinetic results. Understanding the ITG/TE mode driven transport properties of main fuel (deuterium and tritium), ash (helium) and impurities are vital for the prediction of ITER performance. The paper aims to further establish the physics background for this and to provide input to support the validation of reduced physics models aimed at integrated predictive codes.

The remainder of the paper is organised as follows. In Sec. II the fluid and kinetic models used to describe the ITG/TE driven impurity transport are presented. Section III discusses the interpretative analysis of the discharges and the parameter scalings, in particular the scaling with impurity charge number Z, and comparison with experiments. Finally, the conclusions are given in Sec. IV.

## II. IMPURITY TRANSPORT MODELS

### a) Fluid model

The Weiland multi-fluid model [35] is used to describe the ITG/TE mode turbulence and the impurity species. The model equations consist of a set of fluid equations for each species, i.e. ions, trapped electrons and impurities [7-8, 12]. The equations for the perturbations in impurity density, parallel velocity and temperature, neglecting effects of finite impurity Larmor radius, take the form:

$$(\tilde{\omega} + \tau_z^*)\tilde{n}_z - \left(\frac{R}{2L_{nz}} - \lambda\right)\tilde{\phi} + \tau_z^*\tilde{T}_z - \frac{k_\parallel \delta v_{\parallel z}}{\omega_{De}} = 0 \tag{1}$$

$$(\tilde{\omega} - 2\tau_z^*)\frac{k_\parallel \delta v_{\parallel z}}{\omega_{De}} = \frac{Z}{A_z q_*^2}\tilde{\phi} + \frac{\tau_z}{A_z q_*^2}(\tilde{n}_z + \tilde{T}_z) \tag{2}$$

$$\left(\tilde{\omega} + \frac{5}{3}\tau_z^*\right)\tilde{T}_z - \left(\frac{R}{2L_{Tz}} - \frac{1}{3}\frac{R}{L_{nz}}\right)\tilde{\phi} - \frac{2}{3}\tilde{\omega}\tilde{n}_z = 0 \tag{3}$$

Here $\tilde{\phi} = e\phi/T_e$ is the electrostatic potential, $\tilde{n}_z = \delta n_z/n_z$ is the density, $\delta v_{\parallel z}$ is the parallel velocity, $\tilde{T}_z = \delta T_z/T_z$ is temperature, and $\tilde{\omega}=\tilde{\omega}_r+i\tilde{\gamma}$ and $\vec{k}$ are the normalized eigenvalue and wavevector of the unstable ITG/TE modes and tilde denotes normalization with respect to the electron magnetic drift frequency $\omega_{De}$. The normalized gradient scale lengths are defined as $R/L_{nj}= -(R/n_j)(dn_j/dr)$ and $R/L_{Tj}= -(R/T_j)(dT_j/dr)$ where R is the major radius of the tokamak. The other parameters are $\tau_z^*=\lambda T_z/ZT_e$, $\lambda=\cos\theta+s\theta\sin\theta$, $\theta$ is the poloidal angle, $\tau_z = T_z/T_e$, $A_Z = m_z/m_i$ where $m_i$ ($m_z$) is the ion (impurity) mass, s is the magnetic shear, $Z$ is the impurity charge, $q_* = 2qk_\theta\rho_s$, where q is the safety factor, $\rho_s = c_s/\Omega_{ci}$ is the ion sound scale with $\Omega_{ci}=eB/m_i$ and the ion sound speed $c_s = \sqrt{T_e/m_i}$. The curvature terms in Eqs. (1)-(3) enter through the magnetic drift $\omega_{DZ}=\omega_{DZ}(\theta=0)\cdot\lambda$ and originate from the compression of the ExB drift velocity, the diamagnetic drift velocity, and the diamagnetic heat flow. The term proportional to $2\tau_z^*$ in the left hand side of Eq. (2) corresponds to curvature effects from $\vec{\nabla}\cdot\vec{\pi}_z$ (the stress tensor). Combining Eqs. (1)-(3), neglecting the ion pressure perturbations in the parallel ion dynamics for simplicity (Eq. 2), the relation between $\tilde{n}_z$ and $\tilde{\phi}$ can be written as [7]

$$\tilde{n}_z = \left\{\tilde{\omega}\left(\frac{R}{2L_{nz}} - \lambda\right) - \tau_z^*\left(\frac{R}{2L_{Tz}} - \frac{7}{3}\frac{R}{2L_{nz}} + \frac{5\lambda}{3}\right) + \frac{Z}{A_z q_*^2}\left(\frac{\tilde{\omega} + 5\tau_z^*/3}{\tilde{\omega} - 2\tau_z^*}\right)\right\}\frac{\tilde{\phi}}{N} \tag{4}$$

where $N = \tilde{\omega}^2 + \frac{10\tau_z^*}{3}\tilde{\omega} + \frac{5\tau_z^{*2}}{3}$.

The perturbations in impurity, main ion and electron densities are coupled through the quasineutrality condition $\delta n_e/n_e=(1-Zf_Z)\delta n_i/n_i+Zf_Z\delta n_Z/n_Z$ where $f_Z=n_Z/n_e$ is the impurity fraction. Here, the electron response is $\delta n_e/n_e = f_t \delta n_{et}/n_{et} + (1-f_t)\, \delta n_{ef}/n_{ef}$, where $f_t$ is the fraction of trapped electrons. The trapped electron response is calculated using the Weiland fluid model [35] and the free electrons are assumed adiabatic with $\delta n_{ef}/n_{ef}=e\phi/Te$. The linear eigenvalue equation obtained from the quasineutrality condition is solved for an electrostatic potential of general mode width where the magnetic drift $\omega_{Dj}$ and parallel wave number $k_{||}$ are calculated as averages over the poloidal mode structure [8].

From the impurity density response, the quasilinear impurity particle flux can be calculated as $\Gamma_{nz} = -n_z \rho_s c_s \left\langle \tilde{n}_z \frac{\partial \tilde{\phi}}{r \partial \theta} \right\rangle$ $=-D_Z\nabla n_Z+n_Z V_Z$ where $D_Z$ and $V_Z$ are the impurity diffusivity and convective velocity respectively:

$$\frac{\Gamma_{nz}}{n_z c_s} = \frac{k_\theta \rho_s \tilde{\gamma} \left|\tilde{\phi}_k\right|^2}{|N|^2} \left[ \begin{array}{l} \frac{R}{2L_{nz}} \left( |\tilde{\omega}|^2 + \frac{14\tau_z^*}{3}\tilde{\omega}_r + \frac{55\tau_z^{*2}}{9} \right) - \\ \frac{R}{2L_{TZ}} \left( 2\tau_z^* \tilde{\omega}_r + \frac{10\tau_z^{*2}}{3} \right) - \langle \lambda \rangle \left( |\tilde{\omega}|^2 + \frac{10\tau_z^*}{3}\tilde{\omega}_r + \frac{35\tau_z^{*2}}{9} \right) + \\ \frac{Z}{A_z q_*^2 |N_1|^2} \left( \tau_z^* \left( \frac{19}{3}\tilde{\omega}_r^2 - \frac{1}{3}\tilde{\gamma}^2 + \frac{100\tau_z^*}{9}\tilde{\omega}_r - 5\tau_z^{*2} \right) + 2\tilde{\omega}_r |\tilde{\omega}|^2 \right) \end{array} \right] \tag{5}$$

where $N_1 = \tilde{\omega} - 2\tau_z^*$ and <…> represents an average over the poloidal mode structure. The impurity flux is calculated from Eq. (5) by summing over all unstable modes for a fixed length scale of the turbulence. Isotropic turbulence is assumed with $k_r\rho_s=k_\theta\rho_s$, where r and θ are the radial and poloidal coordinates, and the saturated fluctuation level is estimated as $|\phi_k| = \frac{\gamma}{\omega_{*e}} \frac{1}{k_\theta L_{ne}}$ [35]. In Eq. (5), the first term is the diffusive flux and the other terms represent the impurity convective velocity $V_Z$ which includes contributions from three different sources. The first term is called thermodiffusion and is usually outwards ($V_Z>0$) for ITG-modes ($\tilde{\omega}_r<0$) and inwards for TE-modes ($\tilde{\omega}_r>0$). Its leading term scales as $V_Z \sim 1/Z \cdot R/L_{TZ}$ and hence it is negligible for large Z impurities. The second term is the curvature pinch which is proportional to $<\lambda>$ and usually inwards. It is often the dominant term and leads to a positive peaking factor. The third term represents parallel impurity compression [6] and scales as $V_Z \sim Z/A_Z\, k_{\|}^2 \sim Z/(A_Z q^2)$. It is usually inward for ITG-modes and outward for TE-modes. Effects of toroidal rotation would modify the above expression (Eq. 5) and add a new term proportional to the background rotation gradient (roto-diffusion) [19]. These effects may be potentially important in NBI heated tokamak discharges but are not included in the present work. In the trace impurity approximation, the trace species is neglected in the quasi-neutrality condition and in this limit $D_Z$ and $V_Z$ are independent of $\nabla n_Z$. For the trace results presented below, an impurity fraction of $f_Z=10^{-6}$ was typically used.

In steady state plasmas with impurity fuelling through the edge, the zero impurity flux condition $\Gamma_Z = 0$ holds in the core. The balance between outward diffusion and convection $V_Z$ then determines the normalised impurity peaking factor as $PF = -R\nabla n_Z/n_Z = -RV_Z/D_Z$. For inward convection, a peaked impurity profile is obtained with PF>0. For large Z impurities, neglecting parallel impurity compression and assuming a strongly ballooning eigenfunction with $<\lambda>=1$ ($\omega_{DZ}(\theta)\approx\omega_{DZ}(\theta=0)$), the simple analytical result PF=2 is obtained from Eq. 5 by balancing the outward diffusion with the dominant curvature pinch.

### b) Gyrokinetic model

The gyrokinetic results have been obtained with the code GENE [36]. The main part of the simulations have been performed by treating the impurities as a trace species using an impurity fraction of $f_Z=10^{-6}$. The impurity flux is calculated for a few different values of the impurity gradient $\nabla n_Z$ and then the diffusivity $D_Z$ and convective velocity $V_Z$ are obtained assuming a linear dependence between impurity flux and impurity density gradient. In addition, simulations with larger fractions of impurities and with two impurity species present in the plasma have been performed in order to test the validity of the trace impurity approximation for the cases considered. In these simulations, the peaking factor is found by varying impurity gradient until the condition of zero impurity flux is approximately satisfied. Both quasi-linear (QL) and nonlinear (NL) simulations have been performed. The QL simulations calculate the flux from the dominant mode, which is the ITG mode for the JET discharges considered, whereas the fluid and NL

GENE simulations also include the contribution from the subdominant TE mode. The QL simulations assume isotropic turbulence with a fixed length-scale of the turbulence with $k_r\rho_s=k_\theta\rho_s$ as used in the fluid model. A more refined QL kinetic model, not used here, was constructed in [21-22] based on comparisons with NL GENE simulations. The GENE simulations also include impurity FLR effects which are neglected in the fluid case. Impurity FLR effects are expected to be weak and scale as $A_Z/Z$ and should therefore not influence the main results presented in this paper. The NL fluxtube simulations using GENE were performed with a box size of $L_x=L_y=125\rho_S$ with $n_x$ x $n_y$ x $n_z$ = 96x96x32 grid points in real space and $n_v$ x $n_\mu$ = 48x12 in velocity space. Convergence tests were performed linearly and non-linearly to determine an appropriate numerical resolution in all coordinates [36]. Fig. 1 illustrates the results of a nonlinear GENE fluxtube simulation of JET discharge #67730 with parameters taken at r/a=0.5 (see below for parameter values). Figure 1a shows the time evolution of the impurity particle flux and the background density fluctuations. From the time evolution, the time average of the impurity flux is calculated for a few different values of $R/L_{nz}$. The simulations were typically run over the interval $0\leq t(c_s/R)\leq 300$ and the time average was calculated in steady-state for $t(c_s/R)\geq 100$ as indicated in the figure. The result of such a scan is displayed in Fig. 1b where the error bars represent the rms deviations from the average. The scan shows a linear relationship between impurity flux and impurity density gradient and confirms the validity of the trace impurity approximation used here. The space scale of the nonlinear structures relative to the box size is illustrated in Fig. 1c which shows the contour plot of the background density fluctuations in the nonlinear saturated state of Fig. 1a.

## III. SIMULATION RESULTS

The anomalous impurity diffusivity $D_Z$, convective velocity $V_Z$, and normalised impurity peaking factor $PF=-RV_Z/D_Z$ are calculated using the background profiles of JET L-mode discharges #67730 and #67732 [33]. The main parameters are taken from #67730 at r/a=0.5 with $R/L_{Te}=5.6$, $R/L_{Ti}=R/L_{Tz}=5.6$, $f_t=0.55$, $q=2.4$, $s=0.6$, $T_e/T_{i,z}=0.98$, and $R/L_{ne}=2.7$. The other parameters are B=3 T, R=3 m, $T_e=1.55$ keV, and $n_e=1.84\cdot 10^{19}$ $m^{-3}$. The radial profiles of the impurity transport coefficients are calculated and compared with experiments. In addition, the sensitivity of the impurity transport and peaking factors to variations in the plasma parameters around the experimental values are studied. All simulations are performed in a simple s-$\alpha$ equilibrium in the low beta ($\beta \leq 10^{-3}$) electrostatic limit. Effects of non-circular geometry are not included in the present study but have been shown to be rather weak for ITG dominated plasmas using the present fluid model [37-38].

### a) Z-scaling of impurity transport and comparison with experiment

First, the scaling of the normalised impurity density peaking factor $PF=-RV_Z/D_Z$ with impurity charge Z is studied, assuming an impurity mass $A_Z=2Z$. The results obtained with fluid, QL GENE and NL GENE simulations are illustrated in Fig. 2a. The parameters are taken from discharge #67730 at r/a=0.52. For these parameters, the ITG mode is the dominant instability. The kinetic eigenvalues are $\omega_{ITG}=-1.23+i0.43$ and $\omega_{TE}=0.62+i0.28$ (for $k\rho_s=0.3$, $\omega$ is normalized to $\omega_{De}$). The results are shown for 2 different values of the wave-number, $k\rho_s=0.2$ and $k\rho_s=0.3$. For low Z-values, the QL results are quite sensitive to the choice of $k\rho_s$, indicating the difficulty of predicting QL transport based on a single mode. The scaling with Z, with an increase in the peaking factor for small Z, is mainly a result of the thermodiffusive pinch (included here since $\nabla T_Z=\nabla T_i$ is assumed), which is outward for ITG modes and scales as 1/Z. The fluid and GENE results are in good agreement and show a saturation of the peaking factor for large values of Z (Z>10) at a value slightly above the simple analytical fluid result PF=2, which is obtained when neglecting parallel impurity compression. For tungsten (Z=74), the peaking factors are PF=2.18 (fluid) and PF=2.23 (QL GENE) for $k\rho_s=0.3$. For the experimentally more relevant case with partially ionized tungsten, assuming an ionization stage with Z=46+ and $A_Z=184$, we obtain the peaking factor PF=2.06 (fluid) and PF=2.11 (QL GENE), i.e. a downward shift of the peaking factor with about 5%. The ratio $D_Z/\chi_i$ has been calculated using fluid ($k\rho_s=0.3$) and NL GENE simulations. The ratio shows a very weak scaling with Z with $D_Z/\chi_i=1.1$ (fluid) $D_Z/\chi_i\approx 1.0$ (NL GENE) for He.

In Fig. 2b the various contributions to the convective velocity $V_Z$ (in m/s) as a function of Z are illustrated for the same parameters as in Fig. 2a. The results are obtained with the fluid model for wave-number $k\rho_s=0.2$. The results show that the curvature pinch (inward) dominates for all values of Z. The compression term (inward) and the thermopinch (outward) are substantially smaller and have opposite sign as expected from the previous discussion. As observed, the main Z scaling originates from the thermopinch which becomes significant for $Z<10$. The diffusivity $D_Z$ (not shown) is weakly dependent on Z varying from $D_Z=2.6$ m$^2$/s to $D_Z=2.2$ m$^2$/s in going from Z=2 to Z=74.

The NL GENE simulations predict substantially larger turbulent fluctuation levels and hence larger values of $D_Z$ and $V_Z$ than obtained with the fluid model. For He, the NL GENE result is $D_Z=9.1$ m$^2$/s. This is a consequence of the sensitivity of the fluctuation levels to the driving ion temperature gradient and is often observed in fixed gradient simulations of ITG turbulence. However, the peaking factors are much less sensitive to variations in the driving gradient. This is illustrated in Fig. 3a,b which shows the peaking factors for Z=6 and Z=28 and the ion heat diffusivity, versus $R/L_{Ti,z}$, with the other parameters as in Fig. 2a. The stiff behaviour of the ion heat diffusivity $\chi_i$ is apparent in Fig. 3b which shows the $R/L_{Ti,z}$ scaling of $\chi_i$ (in m$^2$/s) obtained with the fluid model. For comparison, the NL GENE result for $\chi_i$ is also shown at the experimental value of the temperature gradient with $R/L_{Ti,z}=5.6$. The impurity peaking factors, however, are only weakly sensitive to variations in the gradients around the experimental values as shown in Fig. 3a. For very weak ion temperature gradients ($R/L_{Ti,z}<4.5$), the TE mode dominates. This results in lower levels of the peaking factors for large Z impurities due to the reversal of the parallel compression pinch [6,13].

Figure 4 a,b,c shows the comparison between the Weiland fluid predictions and experimental results for $D_Z$ (in m$^2$/s) and $V_Z$ (in m/s) and peaking factor $PF=-RV_Z/D_Z$ [30]. The radial profiles of the coefficients are shown for L-mode discharge #67730 (Ne, Ar) and #67732 (Ni). The results are shown for $r/a>0.3$. In the inner core region, the ITG/TE modes are stable according to both fluid and kinetic calculations. Crosses indicate Weiland model predictions whereas dashed lines are neoclassical values. The interpretative comparison used here is very sensitive to the background gradients and a small change of the profiles results in a large change in the diffusivities. This is particularly true close to marginal stability (i.e. for r/a<0.3) which makes comparisons in this region questionable. The region r/a>0.8 is also outside the region of validity, at least for the fluid model used. Hence the comparison with experiments is made around mid-radius. The qualitative trends observed in experiments for Ne, Ar and Ni are reproduced by the theoretical predictions [30]. The calculated diffusivity at mid radius does not scale with Z (from Ne (Z=10) to Ni (Z=28)) and is of the right order of magnitude, two orders of magnitude larger than the neo-classical predictions (Fig. 4a).

The calculated convective velocity is inward (i.e. an impurity pinch) for Z=10-28 and is also of the correct order of magnitude, one order of magnitude larger than neoclassical predictions (Fig. 4b). For Carbon, the predicted peaking with $PF_C=1.9$ (fluid) and $PF_C=1.7$ (NL GENE) is larger than the measured peaking of the C profile which is flat or hollow at mid-radius. This may indicate that the thermodiffusion is larger than predicted by the present models. Alternatively, some of the approximations used in the simulations (trace approximation, collisionless plasma, circular geometry etc) may not be valid for the experimental parameters used. Some of these approximations are examined next.

### b) Trace versus self-consistent treatment

The validity of the trace impurity approximation is investigated in Fig. 5a,b. Fig. 5a displays the normalised impurity density peaking factor $PF=-RV_Z/D_Z$ versus the charge fraction $Z \cdot f_Z$ for Z=6 and Z=18 obtained with the Weiland fluid model and QL GENE simulations. The parameters are the same as in Fig. 2a. As observed, the peaking factors remain close to the trace results ($Zf_Z=0$) for low levels of impurities. The slight increase in the peaking factor for Ar in the fluid case, not seen in the QL GENE simulations, is due to the presence of a subdominant impurity mode which is neglected in the QL GENE simulations which is based on the most dominant mode. The peaking factor obtained using the experimental fraction of Carbon (2% C) is only slightly reduced compared to the trace result of Fig. 2a. This is in line with several previous investigations [5,13,23] which show that the trace approximation is valid for up to 2% C. In Fig. 5b the results for the experimentally relevant case including 2 impurity species is studied. The peaking factor of the trace species with/without a background of 2% Carbon obtained by QL GENE simulations are displayed. The result confirms that the presence of 2% C in the plasma does not significantly modify the trace impurity results of Fig. 2a. We have also performed NL GENE simulations including 2% Carbon to check for possible non-linear effects of the Carbon species on the peaking factor. However, the NL GENE simulations give a peaking factor for Carbon of $PF_C \approx 1.5$ which is close to the NL GENE trace results of Fig. 2a.

### c) Collisions and sheared rotation

The influence of collisions on the results presented is investigated in Fig. 6. The peaking factors for He and C are shown as a function of the normalized effective collision frequency $\nu_{eff}=\nu_{ei}/(\varepsilon\omega_{De})$. The parameters are taken from L-mode discharge #67730 at mid radius which has a relatively high collision frequency with $\nu_{eff}\approx 0.7$. As observed, collisions tend to reduce the peaking factor for low Z impurities. This is expected since the Z=1 background ions are strongly affected by collisions [39]. For Carbon however, the effect is marginal. Larger values of Z (not shown) are less affected [17].

Next, the stabilizing effects of sheared plasma rotation on the ITG/TE mode growth rate is implemented in the impurity transport expressions and the implication for the impurity peaking factor is investigated. This is done by treating the ExB shearing rate $\gamma_E = dV_{ExB}/dr$ as a parameter and applying the Waltz rule [40] to the linear growth rates where $\gamma_{lin}$ is replaced by $\gamma_{net}=\gamma_{lin}-\alpha\gamma_E$ in the fluid transport coefficients (Eq. 5, $\alpha=1$ is used here). The impurity peaking factor versus the shearing parameter $\gamma_E/\gamma_I$ is displayed in Fig. 7 for the same parameters as in Fig. 2a and with $k\rho_s=0.3$. The effective reduction of the ITG growth rate with ExB shearing is found to significantly reduce the peaking factors for low values of impurity charge Z. For Z=2, a flux reversal, from an inward to an outward convective impurity velocity, is obtained for $\gamma_E/\gamma_I\approx 0.25$. The effective reduction of the ITG growth rate leads to a reduction of all contributions to the impurity particle flux in Eq. 5. However, the main effect is that the thermodiffusion is less affected than the other pinch terms resulting in a relative increase of its contribution compared to the other contributions to the impurity transport. Since the thermodiffusion is outward for ITG dominated cases, the result is a reduction (or reversal) of the impurity peaking factor for small values of Z. However, it is found that the experimental value of the shearing parameter at mid radius of JET discharge #67730 is too small ($\gamma_E/\gamma_l \approx 0.1$) to significantly affect the peaking factor for Carbon and hence the flat or hollow C profile obtained in the discharge remains unexplained. We emphasize that the explicit effects of rotation and rotation shear studied in [19] are not included here.

## V. CONCLUSIONS

Impurity transport coefficients driven by ITG/TE mode turbulence were calculated using the Weiland multi-fluid model as well as quasi-linear and nonlinear gyrokinetic simulations using the code GENE. The analysis was performed using profile data from dedicated impurity injection experiments at JET. The sign of the impurity convective velocity (pinch) and the dependence of the impurity transport coefficients and impurity density peaking factor $PF=-R\nabla n_z/n_z$ on plasma parameters, in particular the impurity charge number Z, were studied. It was shown that the fluid, quasilinear and nonlinear gyrokinetic simulations predict similar impurity behaviour for the considered ITG mode dominated L-mode discharges. The impurity peaking factors were found to increase with Z for low Z-values ($Z \leq 10$) and saturate at moderate values of the impurity peaking factor for large values of Z. The saturated peaking factors for $Z >> 1$ were found to be substantially smaller than the neo-classical predictions with typically $2 < PF \leq 3$. The results are in qualitative agreement with the experimental findings at mid-radius for the injected impurities Ne, Ar, and Ni. For Carbon however, the predicted peaking is substantially larger than the peaking obtained from the measured profile which is flat or even hollow. Various effects that could potentially explain this discrepancy between theory and experiment were investigated. The effect of sheared plasma rotation was included by implementing the Waltz rule $\gamma_{net}=\gamma_{lin}-\gamma_E$ in the Weiland transport model (Eq. 5), where $\gamma_E = dV_{ExB}/dr$ is the shearing rate. Sheared plasma flows were found to have a significant effect of the impurity peaking factor for low Z impurities ($Z<10$) where a reduction or even a reversal (for He) of the impurity peaking was obtained. The reduction of the peaking factor is a result of the increased relative contribution from thermodiffusion in cases where the ITG growth rate is reduced by ExB shearing. Also effects of collisions and 2% background Carbon (vs trace) were found to reduce the low Z peaking factors. However, these effects were not sufficient to significantly reduce the Carbon peaking factor for the studied L-mode experimental parameters values. The results may indicate that some important ingredient is missing in the models used. Work is in progress in order to investigate if the effects of roto-diffusion [19] are as significant for the interpretation of low Z impurity transport at JET as indicated by recent analysis of AUG experiments [41]. Effects of realistic tokamak geometry will also be included. In addition, the computationally efficient fluid model will be used in predictive transport code simulations of JET discharges, allowing for the self-consistent evolution of temperature, density, momentum and impurity profiles.

## ACKNOWLEDGEMENT

This work was supported by EURATOM and carried out within the framework of the European Fusion Development Agreement. The views and opinions expressed herein do not necessarily reflect those of the European Commission.

## REFERENCES

1. G. F. Matthews et al, *Phys. Scr.* **T138** (2009).
2. E. A. Belli and J. Candy, *Plasma Phys. Controlled Fusion* **50**, 095010 (2008).
3. S. P. Hirshman and D. J. Sigmar, *Nucl. Fusion* **21**, 1079 (1981).
4. P. Helander and D. J. Sigmar, *Collisional Transport in Magnetized Plasmas* Cambridge University Press, Cambridge, (2002).
5. C. Estrada-Mila, J. Candy, and R. E. Waltz, *Phys. Plasmas* **12**, 022305 (2005).
6. C. Angioni and A. G. Peeters, *Phys. Rev. Lett.* **96**, 095003 (2006).
7. H. Nordman, R. Singh, T. Fülöp, L.-G. Eriksson, R. Dumont, J. Anderson, P. Kaw, P. Strand, M. Tokar, and J. Weiland, *Phys. Plasmas* **15**, 042316 (2008).
8. H. Nordman, T. Fülöp, J. Candy, P. Strand, and J. Weiland, *Phys. Plasmas* **14**, 052303 (2007).
9. N. Dubuit, X. Garbet, T. Parisot, R. Guirlet, and C. Bourdelle, *Phys. Plasmas* **14**, 042301 (2007).
10. R. Guirlet, C. Giroud, T. Parisot, M. E. Puiatti, C. Bourdelle, L. Carraro, N. Dubuit, X. Garbet, and P. R. Thomas, *Plasma Phys. Controlled Fusion* **48**, B63 (2006).
11. T. Fülöp and J. Weiland, *Phys. Plasmas* **13**, 112504 (2006).
12. M. Fröjdh, M. Liljeström, and H. Nordman, *Nucl. Fusion* **32**, 419 (1992).
13. T. Fülöp, H. Nordman, *Phys. Plasmas* **16**, 032306 (2009).
14. C. Angioni, A. G. Peeters, G. V. Pereverzev et al, *Nucl. Fusion* **49**, 055013 (2009).
15. C. Angioni, L. Carraro, T. Dannert et al., *Phys. Plasmas* **14**, 055905 (2007).
16. T. Hein and C. Angioni, *Phys. Plasmas* **17**, 012307 (2010).
17. T. Fülöp, S. Braun, I. Pusztai, *Phys. Plasmas* **17**, 062501 (2010).
18. S. Futatani, X. Garbet, S. Benkadda and N. Dubuit, *Phys. Rev. Lett.* **104**, 015003 (2010).
19. Y. Camenen, A.G. Peeters, C. Angioni, et al., *Phys. Plasmas* **16**, 012503 (2009).
20. C. Bourdelle, X. Garbet, F. Imbeaux, et al., *Phys. Plasmas* **14**, 112501 (2007).
21. T. Dannert and F. Jenko, *Phys. Plasmas* **12**, 072309 (2005).
22. F. Merz and F. Jenko, *Phys. Rev. Lett.* **100**, 035005 (2008).
23. C. Angioni and A.G. Peeters, *Phys. Plasmas* **15**, 052307 (2008).
24. R. Basu, T. Jessen, V. Naulin, J. Juul Rasmussen, *Phys. Plasmas* **10**, 2696 (2003).

25. V. Naulin, *Phys. Rev. E* **71**, 015402 (2005).

26. M. Priego, O.E. Garcia, V. Naulin, J. Juul Rasmussen, *Phys. Plasmas* **12**, 062312 (2005).

27. R. Dux, R. Neu, A. G. Peeters, G. Pereverzev, A. Mück, F. Ryter, J. Stober, *Plasma Phys. Controlled Fusion* **45**, 1815 (2003).

28. M. E. Puiatti, M. Valisa, C. Angioni, L. Garzotti, P. Mantica, M. Mattioli, L. Carraro, I. Coffey, and C. Sozzi, *Phys. Plasmas* **13**, 042501 (2006).

29. M. E. Puiatti, M. Valisa, M. Mattioli, T. Bolzonella, A. Bortolon, I. Coffey, R. Dux, M. von Hellermann, P. Monier-Garbet, M. F. F. Nave, J. Ongena, *Plasma Phys. Controlled Fusion* **45**, 2011 (2003); M. F. F. Nave, J. Rapp, T. Bolzonella, *Nuclear Fusion* **43**, 1204 (2003).

30. L. Carraro, C. Angioni, C. Giroud, M. E. Puiatti, M. Valisa, P. Buratti, R. Buttery, I. Coffey, L. Garzotti, D. Van Eester, L. Lauro Taroni, K. Lawson, E. Lerche, P. Mantica, M. Mattioli, V. Naulin, Proceedings of 34th EPS Conference on Controlled Fusion and Plasma Physics, Warszawa 2007, Vol. **31 A**.

31. C. Giroud, C. Angioni, L. Carraro, et al, Proceedings of 34th EPS Conference on Controlled Fusion and Plasma Physics, Warszawa 2007, Vol. **31 F**, P-2.049.

32. S. Günter, C. Angioni, M. Apostoliceanu, et al, *Nucl. Fusion* **45**, S98 (2005).

33. C. Giroud et al., 12th International Workshop on "H-mode Physics and Transport Barriers", September 30-October 2 2009, Princeton, USA.

34. C. Giroud, R. Barnsley, P. Buratti et al, Nucl. Fusion **47**, 313 (2007).

35. J. Weiland, *Collective Modes in Inhomogeneous Plasma* IOP, Bristol, (2000).

36. F. Jenko et al., *Physics of Plasmas* **7**, 1904 (2000); F. Merz, PhD Thesis, Münster University (2008); see also: www.ipp.mpg.de/~fsj/gene.

37. J. Anderson, H. Nordman, J. Weiland, *Plasma Phys. Controlled Fusion* **42**, 545 (2000).

38. J. Anderson, T. Rafiq, M. Nadeem, M. Persson, *Phys. Plasmas* **9**, 1629 (2002).

39. C. Angioni, J. Candy, E. Fable et al., *Phys. Plasmas* **16**, 060702 (2009).

40. R.E. Waltz et al., *Phys. Plasmas* **1**, 2229 (1994).

41. C. Angioni et al., submitted to *Nucl. Fusion* (2010).

Figure Captions

Fig. 1a Time traces of the impurity particle flux (in units of $10^6 c_s \rho_{ref}^2 n_e/R^2$) and ion density fluctuations $n_D^2$ (in units of $n_e^2 \rho_{ref}^2/R^2$) obtained from NL GENE fluxtube simulations in the trace impurity limit (collisionless, electrostatic). The parameters are taken from JET Pulse No: 67730 ($I=1.8MA, B_T=3T, P_{NBI} = 4.2MW$) at $r/a \approx 0.5$ with $Z=42$, $R/L_{nz}=2.6$, $R/L_{ne}=2.7$, $R/L_{Tj}=5.6, T_e/T_i=1$, $q=2.4$, and $s=0.6$.

Fig. 1b Time averaged impurity particle flux (in units of $c_s \rho_{ref}^2 n_e/R^2$) versus $R/L_{nz}$ for $Z=42$. Results obtained from NL GENE simulations with parameters from Fig. 1a.

Fig. 1c Contour plot of background ion density fluctuations obtained in the non-linear saturated state of Fig. 1a, at $t \sim 300\ R/c_s$.

Fig. 2a Scaling of normalised impurity density peaking factor $PF=-RV_Z/D_Z$ with impurity charge Z for $Z \geq 2$ for wave-numbers $k\rho_s=0.2$ and $k\rho_s=0.3$. Results from Weiland fluid model and QL and NL GENE simulations are compared in the trace impurity limit (collisionless, electrostatic). The parameters are taken from JET Pulse No: 67730 at $r/a \approx 0.5$.

Fig. 2b Scaling of impurity convective velocity $V_Z$ with Z. Results from Weiland fluid model with $k\rho_s=0.2$. The parameters are the same as in Fig. 2a.

Fig. 3a Peaking factors for C and Ni versus the driving gradient $R/L_{Ti,z}$. Results from QL GENE and Weiland fluid model with $k\rho_s=0.2$. The other parameters are the same as in Fig. 2a.

Fig. 3b Ion heat diffusivity $\chi_i$ (in $m^2/s$) versus the driving gradient $R/L_{Ti,z}$.for the same case as in Fig. 3a. Results from Weiland fluid model with $k\rho_s=0.2$ and NL GENE simulations.

Fig. 4 a,b,c Comparison between the Weiland fluid predictions and experimental results for $D_Z$ ($m^2$/s, a), $V_Z$ (m/s, b) and $PF=-RV_Z/D_Z$ (c). The radial profiles of the coefficients are shown for L-mode Pulse No's: 67730 (Ne, Ar) and #67732 (Ni). Crosses indicate Weiland model predictions whereas dashed lines are neoclassical values.

Fig. 5a Normalised impurity density peaking factor $PF=-RV_Z/D_Z$ versus charge fraction $Z \cdot f_Z = Z \cdot n_Z/n_e$ for Z=6 and Z=18. Comparison between Weiland fluid model and QL GENE simulations. Parameters taken from Pulse No: 67730 at $r/a \approx 0.5$. The experimental value for the Carbon charge fraction is $Z \cdot f_Z \approx 0.12$.

Fig. 5b Normalised impurity density peaking factor $PF=-RV_Z/D_Z$ versus Z in the trace impurity limit compared to a case with two impurity species; one trace species in the presence of 2% C which is included self-consistently. Results obtained by QL GENE simulations. The parameters are the same as in Fig. 2a.

Fig. 6 Normalised impurity density peaking factor $PF=-RV_Z/D_Z$ versus normalised effective collision frequency $\nu_{eff}=\nu_{ei}/(\varepsilon\omega_{De})$ for Z=2 and Z=6. The parameters are the same as in Fig. 2a.

Fig. 7 Normalised impurity density peaking factor $PF=-RV_Z/D_Z$ versus shearing parameter $\gamma_E/\gamma_l$ for the same parameters as in Fig. 2a. The results are obtained using the Weiland fluid model for $k\rho_s=0.3$.

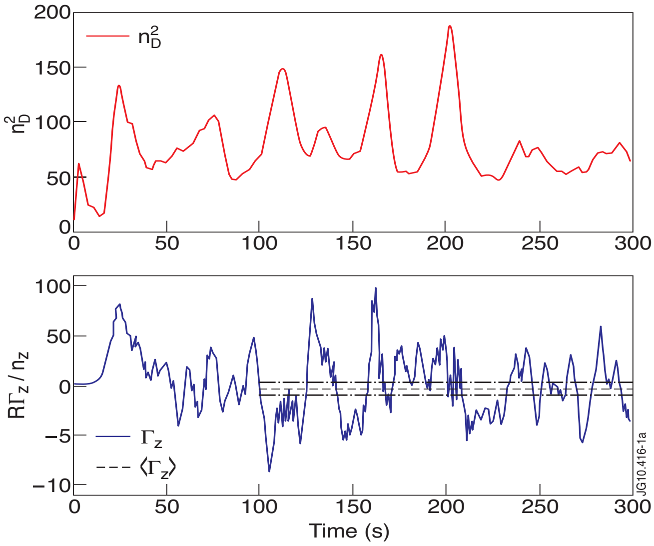
200
150
100
50
0
$n_D^2$
$n_D^2$
0
50
100
150
200
250
300
100
50
0
−5
−10
$R\Gamma_z / n_z$
$\Gamma_z$
$\langle\Gamma_z\rangle$
0
50
100
150
200
250
300
Time (s)
JG10.416-1a

Fig. 1a

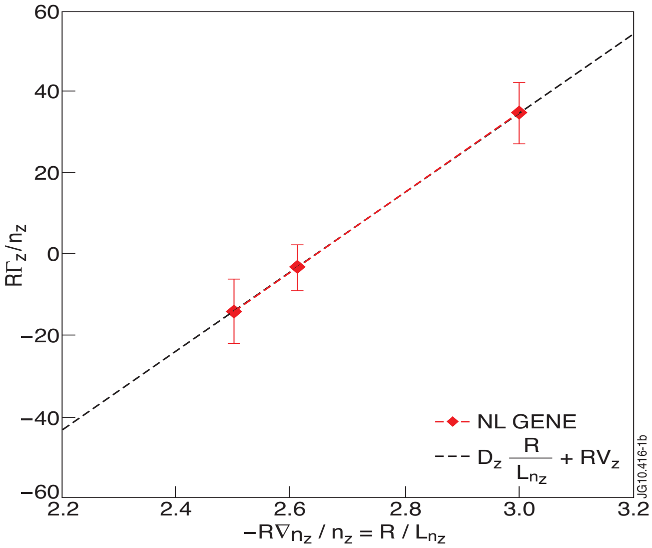
60
40
20
0
−20
−40
−60
$R\Gamma_z/n_z$
NL GENE
$D_z \frac{R}{L_{n_z}} + RV_z$
2.2
2.4
2.6
2.8
3.0
3.2
$-R\nabla n_z / n_z = R / L_{n_z}$
JG10.416-1b

Fig. 1b

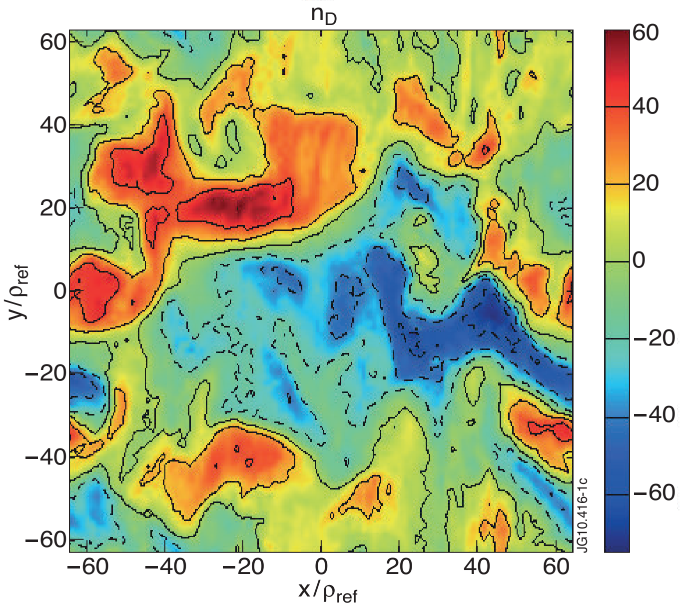
n_D
60
40
20
0
−20
−40
−60
y/ρ_ref
x/ρ_ref
JG10.416-1c

Fig. 1c

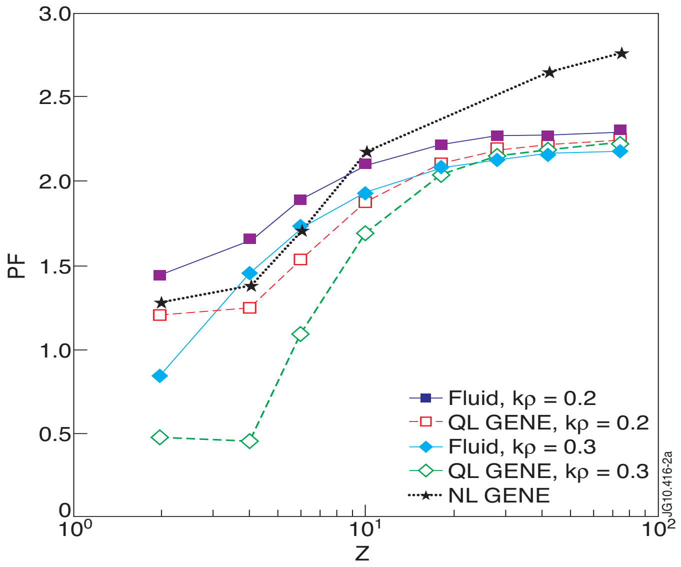
PF
Z
3.0
2.5
2.0
1.5
1.0
0.5
0
10^0
10^1
10^2
Fluid, kρ = 0.2
QL GENE, kρ = 0.2
Fluid, kρ = 0.3
QL GENE, kρ = 0.3
NL GENE
JG10.416-2a

Fig. 2a

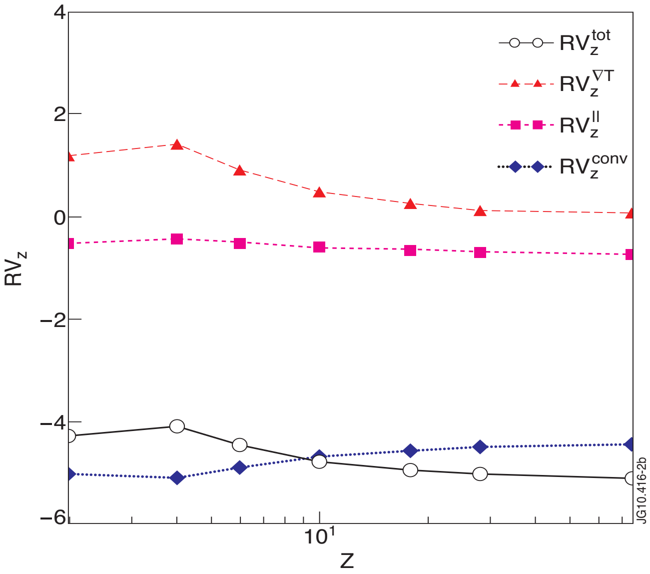
RV$_z^{tot}$
RV$_z^{\nabla T}$
RV$_z^{ll}$
RV$_z^{conv}$
RV$_z$
4
2
0
−2
−4
−6
10$^1$
Z
JG10.416-2b

Fig. 2b

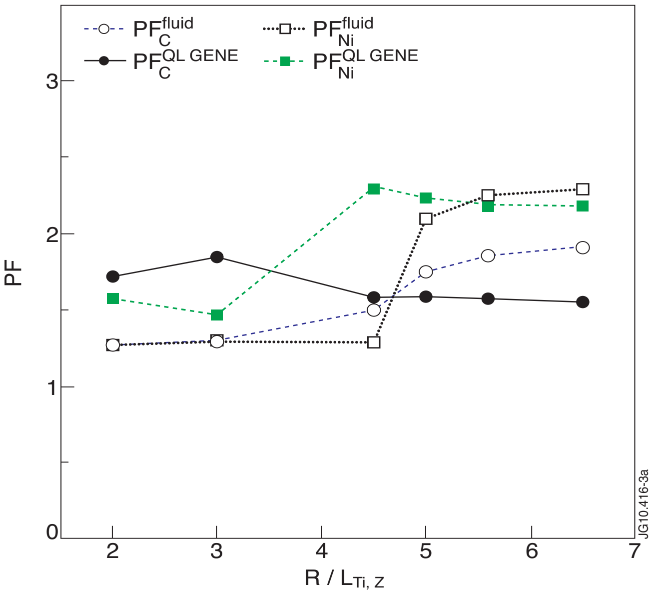
PF$_C^{fluid}$
PF$_{Ni}^{fluid}$
PF$_C^{QL\ GENE}$
PF$_{Ni}^{QL\ GENE}$
PF
3
2
1
0
2
3
4
5
6
7
R / L$_{Ti, Z}$
JG10.416-3a

Fig. 3a

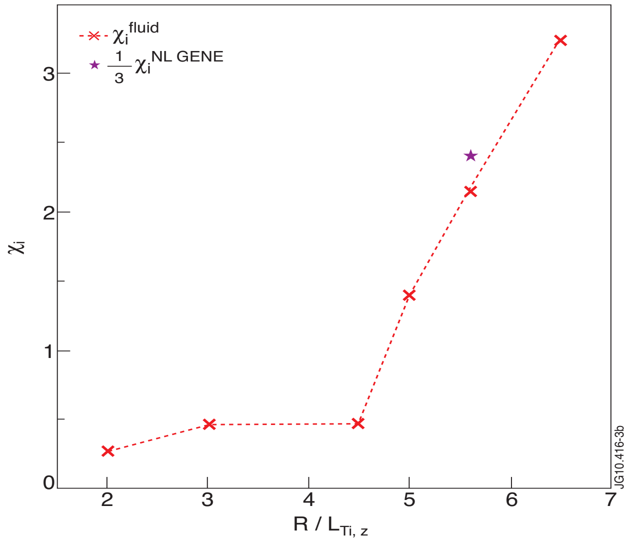
$\chi_i^{fluid}$
$\frac{1}{3}\chi_i^{NL\ GENE}$
$\chi_i$
0
1
2
3
2
3
4
5
6
7
$R / L_{Ti,z}$
JG10.416-3b

Fig. 3b

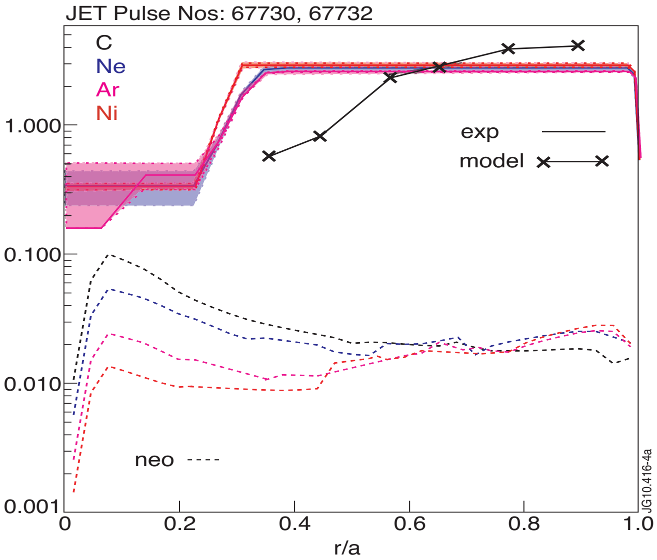
JET Pulse Nos: 67730, 67732
C
Ne
Ar
Ni
exp
model
neo
1.000
0.100
0.010
0.001
0
0.2
0.4
0.6
0.8
1.0
r/a
JG10.416-4a

Fig. 4a

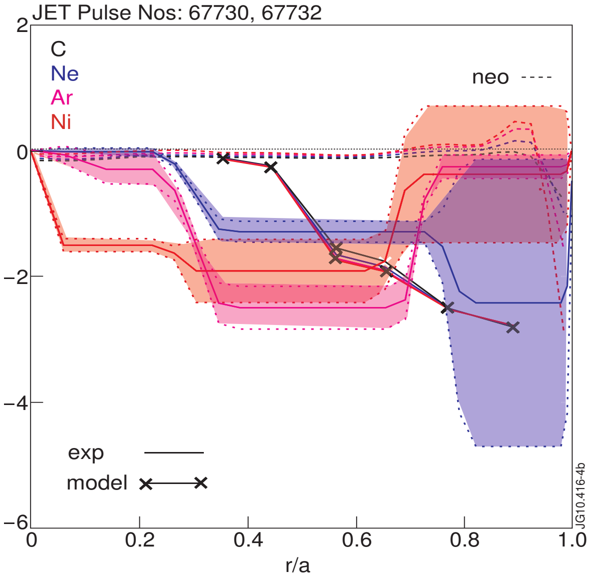
JET Pulse Nos: 67730, 67732
C
Ne
Ar
Ni
neo
exp
model
JG10.416-4b
2
0
−2
−4
−6
0
0.2
0.4
0.6
0.8
1.0
r/a

Fig. 4b

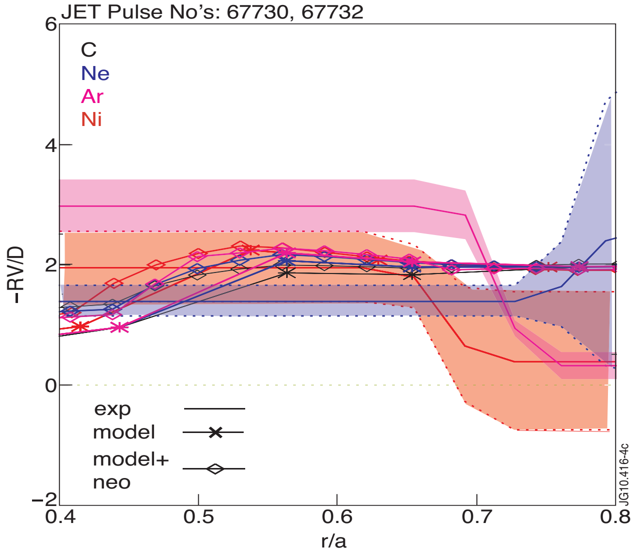
JET Pulse No's: 67730, 67732
C
Ne
Ar
Ni
−RV/D
exp
model
model+
neo
JG10.416-4c
6
4
2
0
−2
0.4
0.5
0.6
0.7
0.8
r/a

Fig. 4c

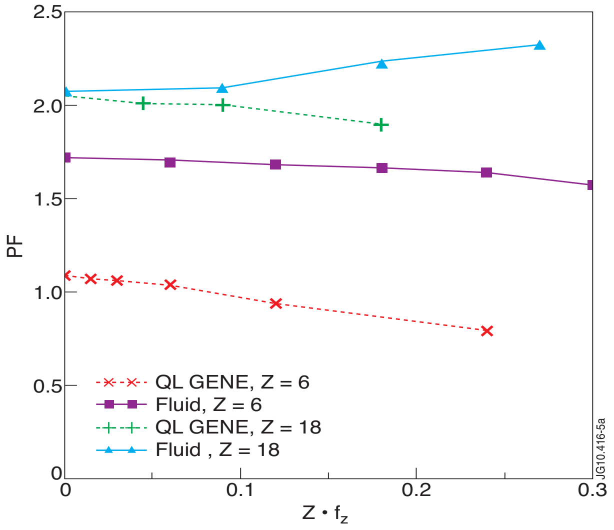
PF
2.5
2.0
1.5
1.0
0.5
0
0
0.1
0.2
0.3
Z • $f_z$
QL GENE, Z = 6
Fluid, Z = 6
QL GENE, Z = 18
Fluid , Z = 18
JG10.416-5a

Fig. 5a

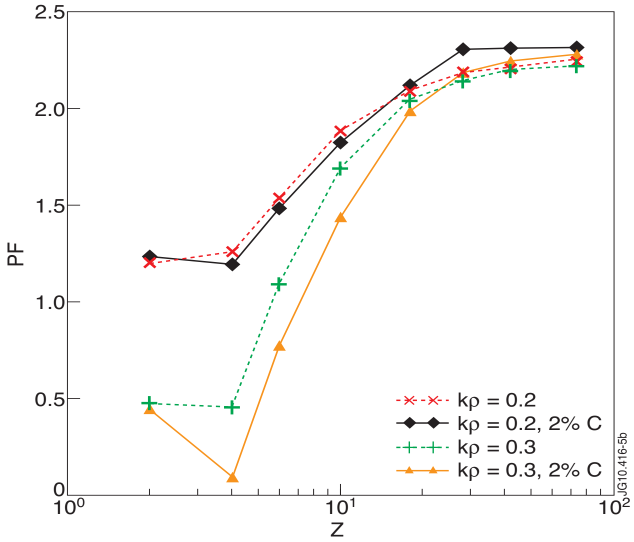
PF
2.5
2.0
1.5
1.0
0.5
0
$10^0$
$10^1$
$10^2$
Z
kρ = 0.2
kρ = 0.2, 2% C
kρ = 0.3
kρ = 0.3, 2% C
JG10.416-5b

Fig. 5b

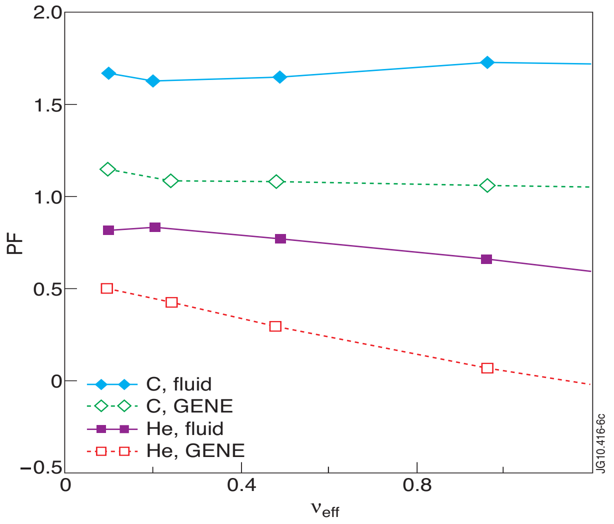
2.0
1.5
1.0
0.5
0
−0.5
PF
0
0.4
0.8
$\nu_{eff}$
C, fluid
C, GENE
He, fluid
He, GENE
JG10.416-6c

Fig. 6

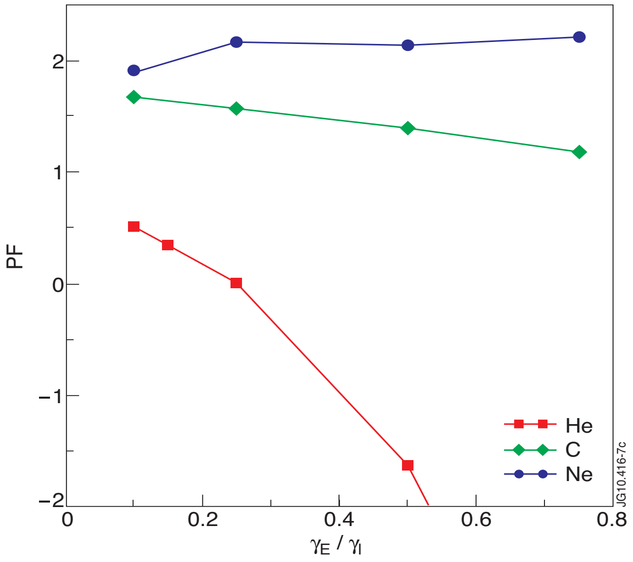
2
1
0
−1
−2
PF
0
0.2
0.4
0.6
0.8
$\gamma_E / \gamma_I$
He
C
Ne
JG10.416-7c

Fig. 7